

# Identification of a novel neutralization epitope in rhesus AAVs

Gabriel Dagotto,<sup>1</sup> Jana L. Fisher,<sup>1</sup> David Li,<sup>1</sup> Zhenyu Li,<sup>1</sup> Simon Jenni,<sup>2</sup> Zongli Li,<sup>2</sup> Lawrence J. Tartaglia,<sup>3</sup> Peter Abbink,<sup>1</sup> and Dan H. Barouch<sup>1,4</sup>

<sup>1</sup>Center for Virology and Vaccine Research, Beth Israel Deaconess Medical Center, Harvard Medical School, Boston, MA 02215, USA; <sup>2</sup>Department of Biological Chemistry and Molecular Pharmacology, Harvard Medical School, 250 Longwood Avenue, Boston, MA 02115, USA; <sup>3</sup>Department of Biological Sciences, Lehigh University, Bethlehem, PA 18015, USA; <sup>4</sup>Ragon Institute of MGH, MIT, and Harvard, Cambridge, MA 02139, USA

**Adeno-associated viruses (AAVs) are popular gene therapy delivery vectors, but their application can be limited by anti-vector immunity. Both preexisting neutralizing antibodies (NAbs) and post-administration NAbs can limit transgene expression and reduce the clinical utility of AAVs. The development of novel AAVs will advance our understanding of AAV immunity and may also have practical applications. In this study, we identified five novel AAV capsids from rhesus macaques. RhAAV4282 exhibited 91.4% capsid sequence similarity with AAV7 and showed similar tissue tropism with slightly diminished overall signal. Despite this sequence homology, RhAAV4282 and AAV7 showed limited cross-neutralization. We determined a cryo-EM structure of the RhAAV4282 capsid at 2.57 Å resolution and identified a small segment within the hypervariable region IV, involving seven amino acids that formed a shortened external loop in RhAAV4282 compared with AAV7. We generated RhAAV4282 and AAV7 mutants that involved swaps of this region and showed that this region partially determined neutralization phenotype. We termed this region the hypervariable region IV neutralizing epitope (HRNE). Our data suggests that modification of the HRNE can lead to AAVs with altered neutralization profiles.**

## INTRODUCTION

Adeno-associated viruses (AAV) have been found to have multiple attractive qualities for gene therapy. AAVs have low immunogenicity,<sup>1</sup> long expression times,<sup>2,3</sup> broad tissue tropism,<sup>4,5</sup> and are mostly non-pathogenic.<sup>6</sup> AAVs have been used to generate multiple drugs currently in clinical trials for genetic diseases.<sup>7</sup>

Although AAVs are considered some of the best vectors for gene therapy, they also have limitations: broad tissue tropism is useful in some cases but can be problematic due to liver toxicity,<sup>8</sup> and preexisting immunity as well as anti-vector immunity following treatment can limit the therapeutic efficacy of AAVs.<sup>1,9–13</sup> To overcome humoral immunity, researchers often exclude patients with anti-vector antibodies or immunosuppress them.<sup>14,15</sup> AAVs typically have durable expression in humans, but in some cases a second AAV dose is needed to maintain therapeutic efficacy.<sup>16–19</sup> Administering follow-up AAV doses

can be problematic as many patients develop antibodies against the AAV capsid used in the first dose.<sup>15</sup>

To address these problems, it is important to expand the repertoire of available AAV capsids. Previous work from our group investigated the effects of simian immunodeficiency virus (SIV)-mediated immunodeficiency on the enteric virome of rhesus macaques.<sup>20</sup> This work demonstrated that rhesus macaques infected with SIV showed higher numbers of viral reads in numerous virus families such as *Adenoviridae*, *Picornaviridae*, and *Parvoviridae*. We decided to further investigate the *Parvoviridae* reads with the goal of identifying novel AAV capsids. We discovered five novel AAV capsid sequences that we used to generate vectors. We then further characterized the best growing virus, RhAAV4282, which is closely related to AAV7, and we identified a neutralizing epitope that we called hypervariable region IV neutralizing epitope (HRNE).

## RESULTS

### Discovery of novel AAV capsids

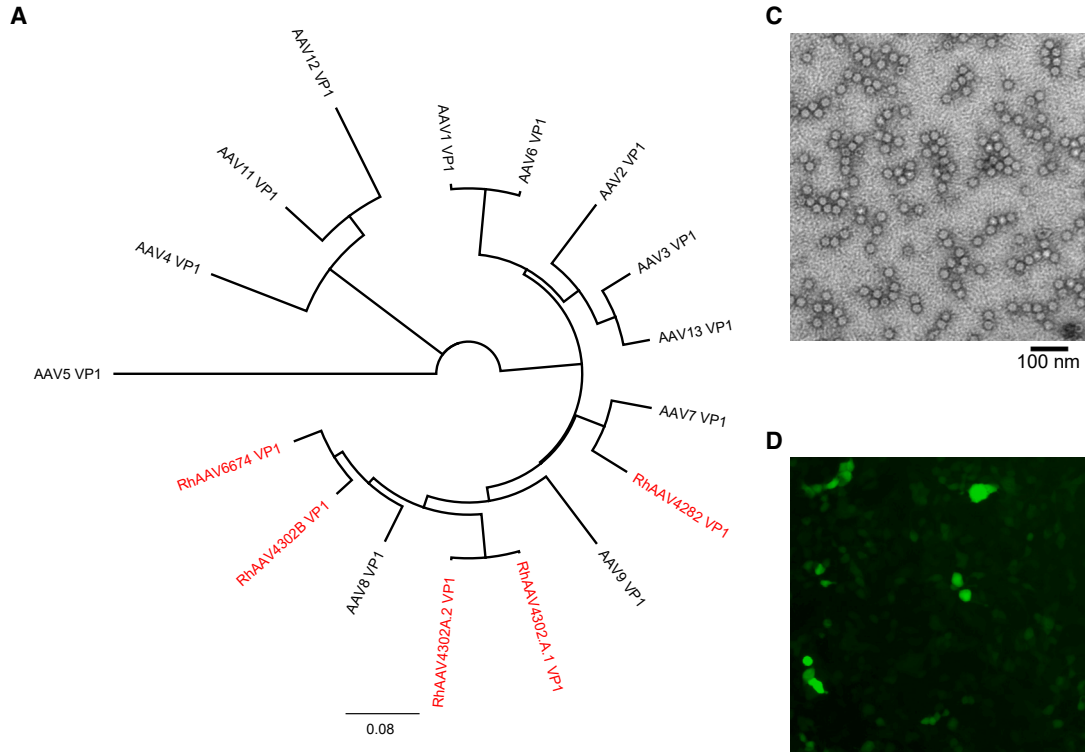
We previously reported that SIV-infected rhesus macaques (*Macaca mulatta*) had increased viral reads in stool samples in many viral families, including *Parvoviridae*.<sup>20</sup> To investigate whether these samples included new AAV capsids, we analyzed stool samples from rhesus macaques that had tested positive for parvoviruses.<sup>20</sup> The stool was filtered and then used to infect human E1-complementing cells. Cells were monitored for cytopathic effects (CPEs) as indicative of helper virus necessary for AAV replication. If CPEs were observed, then cell supernatants were harvested and subjected to PCR amplification using degenerative AAV capsid primers targeting the capsid genes (VP1, VP2, and VP3) of AAVs. PCR products were sequenced and then cloned into AAV2 RepCap plasmids. Five novel capsids were discovered: RhAAV4282, RhAAV4302A.1, RhAAV4302A.2, RhAAV4302B, and RhAAV6674.

Received 14 May 2024; accepted 30 September 2024;  
<https://doi.org/10.1016/j.omtm.2024.101350>.

**Correspondence:** Dan H. Barouch, Center for Virology and Vaccine Research, Beth Israel Deaconess Medical Center, Harvard Medical School, Boston, MA 02215, USA.

**E-mail:** [dbarouch@bidmc.harvard.edu](mailto:dbarouch@bidmc.harvard.edu)





**B**

**Capsid Percent Similarity**

	RhAAV4282	RhAAV4302A.1	RhAAV4302A.2	RhAAV4302B	RhAAV6647
AAV1	84.8	84	83.9	83.9	82.4
AAV2	81.3	82.4	82.2	83.2	82.6
AAV3	84	84	83.9	85.6	83.9
AAV4	56.1	55.8	55.8	56.9	57.2
AAV5	48.9	46.3	46.3	47	46.7
AAV6	84.6	84	83.9	84.1	82.6
AAV7	91.4	86.9	86.7	87.2	87.2
AAV8	86.5	89.7	89.5	91.6	92.8
AAV9	79.8	85.5	85.3	85.2	84.2
AAV11	60.5	59.7	59.4	60	58.7
AAV12	55.9	53.9	53.5	53.6	53.8
AAV13	84.6	83.7	83.7	86.2	85
RhAAV4282	100	85.4	85.7	88.5	87.5
RhAAV4302A.1	85.4	100	99.7	93.2	89.5
RhAAV4302A.2	85.7	99.7	100	93.1	89.7
RhAAV4302B	88.5	93.2	93.1	100	94.8
RhAAV6647	87.5	89.5	89.7	94.8	100

(legend on next page)

Phylogenetic analysis of the capsid VP1 protein showed that RhAAV4282 was closely related to AAV7, whereas RhAAV4302A.1, RhAAV4302A.2, RhAAV4302B, and RhAAV6674 were more closely related to AAV8 and AAV9 (Figure 1A). All five capsids shared >85% amino acid similarity among themselves, although RhAAV4282 was the most divergent capsid among the five isolates. The RhAAV4282 VP1 protein shared 91.4% protein sequence similarity to AAV7 VP1, with only 65 amino acid differences. RhAAV4302A.1 (89.7%), RhAAV4302A.2 (89.5%), RhAAV4302B (91.6%), and RhAAV6674 (92.8%) all shared most sequence homology with AAV8 (Figure 1B). We decided to further characterize RhAAV4282 as it was the most divergent capsid and showed the highest production titers. We were able to generate functional vectors with normal size (25 nm diameter) and shape for RhAAV4282 (Figure 1C), and these vectors had the capacity to infect cells as measured by EGFP expression (Figure 1D).

### Biochemical characterization

We first tested RhAAV4282 cell transduction efficacy compared to closely related AAV7 and commonly used AAV9 (Figure S1) and observed similar transduction efficiency in all cell lines tested. We then tested RhAAV4282 using *in vitro* methods to determine whether it used common AAV receptors and attachment factors for cellular entry. We tested two of the most common AAV attachment factors, heparin sulfate and sialic acid, as well as the AAV receptor (AAVR) (KIAA0319L).<sup>21,22</sup> For these tests, we used RhAAV4282 expressing EGFP. To test heparin sulfate usage, we treated 293T cells with increasing levels of heparinase III enzyme. If heparin sulfate was used for entry there would be a dose-dependent decrease in %GFP<sup>+</sup> cells. We observed this decrease in AAV2.eGFP (Figure S2), a known heparin sulfate using AAV, but we did not observe a decrease in RhAAV4282 (Figure 2A). We tested sialic acid usage by using a cell line with cytidine monophosphate *N*-acetylneuraminic acid synthetase (CMAS) knocked out. CMAS is a sialic acid transporter, and knockout removes sialic acid from the cell surface.<sup>23,24</sup> Depletion of sialic acid also indirectly tests for the use of galactose, as removal of sialic acid exposes more galactose, leading to an increase in transduction by AAVs using galactose as an attachment factor.<sup>25</sup> CMAS-knockout (KO) cells showed a decrease in AAV1 GFP signal (sialic acid virus<sup>26</sup>) and an increase in AAV9 GFP signal (galactose virus<sup>25,27</sup>) (Figure S3) but no difference in RhAAV4282 transduction (Figure 2B). In contrast, KO of the AAVR resulted in nearly complete loss of transduction by RhAAV4282 and other control viruses (Figure 2C) (Figure S4). These results show that RhAAV4282, like the vast majority of AAVs, uses the AAVR for entry. Similar to the closely related AAV7,<sup>28</sup> the attachment factor for RhAAV4282 is unknown.

AAVs are generally thermostable, but the stability of the capsid can vary significantly based on serotype. RhAAV4282 capsid thermosta-

bility was tested by differential scanning fluorimetry. AAV particles were mixed with SYPRO Orange dye and then heated while detecting fluorescent signal. As the AAV capsid denatures due to increased temperature, fluorescent signal can be detected to determine the melting temperature ( $T_m$ ) of the capsid. RhAAV4282 ( $T_m = 71.1^\circ\text{C}$ ) was found to have nearly the same melting temperature as its close relative AAV7 ( $T_m = 71.2^\circ\text{C}$ ) (Figure 2D). AAV9 instead showed a more stable capsid with a  $T_m$  of  $78.2^\circ\text{C}$ .

### Human seroprevalence

Anti-AAV antibodies can be a major limitation in gene therapy administration. Over 70% of the population is thought to be seropositive for AAV2, and the seroprevalence of other commonly used AAVs is high.<sup>12,29,30</sup> To investigate the seroprevalence of RhAAV4282 in the general population, we used 69 Boston patient samples from our hospital biorepository to measure neutralizing antibody (NAb) titers against RhAAV4282, closely related AAV7, and human virus AAV2. We observed no neutralization in ~80% of patients for RhAAV4282, AAV7, and AAV2 (Figure 3A). Among the individuals who showed neutralization, we observed the highest NAb titers against AAV2. RhAAV4282 was found to have the lowest NAb titers of the three viruses tested (Figure 3B) (Figures S5–S7). We observed no clear differences in sex or age comparing positive and negative patients (Table S1).

### Innate immune response

To further characterize RhAAV4282, we measured early innate immune responses after injection of mice with RhAAV4282, AAV7, and AAV9 vectors expressing a luciferase transgene. Serum cytokine levels were measured at the following time points: 0, 2, 6, 24, 48, and 72 h. We found that RhAAV4282 exhibited a unique innate immune profile, although RhAAV4282 was surprisingly more similar to AAV9 than AAV7. For interferon- $\gamma$  (IFN- $\gamma$ ) (Figure S8A), interleukin-10 (IL-10) (Figure S8B), IFN- $\gamma$ -inducible protein-10 (IP-10) (Figure S8C), and monocyte chemoattractant protein-1 (MCP-1) (Figure S8D), RhAAV4282 closely matched AAV9 instead of AAV7. The other measured cytokines showed no discernible differences between AAVs (Figure S9).

### Tissue tropism

We next explored RhAAV4282 tissue tropism *in vivo*. RhAAV4282, AAV7, and AAV9 expressing a luciferase transgene were administered to BALB/c mice intravenously. Four weeks later, whole-mouse *in vivo* imaging system (IVIS) imaging was used to determine transduction. Quadriceps, liver, diaphragm, and heart tissues were harvested to quantify tissue-specific signal differences between the tested AAVs. After determining luciferase signal, tissues were processed to extract nucleic acids to determine the DNA and RNA localization in each tissue. DNA was extracted from select tissues, and genome

### Figure 1. Discovery of novel AAV capsids in SIV-infected rhesus macaques

(A) Phylogenetic tree of novel rhesus AAVs discovered in this study (red) and contemporary AAV serotypes (black). Scale bar represents mean number of amino acid changes per site. (B) Capsid percent similarity between contemporary serotypes and novel AAV capsids. (C) Negative stain EM of RhAAV4282 capsid packaging a luciferase transgene. (D) *In vitro* transduction of 293T cells with RhAAV4282 expressing EGFP.

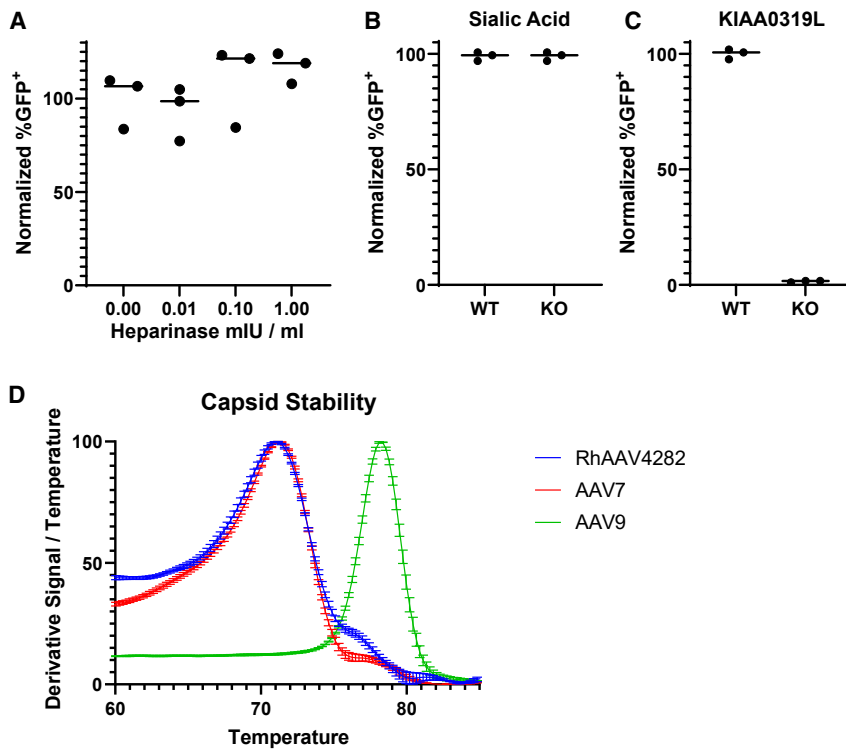


**Figure 2. In vitro receptor and capsid testing**

(A) Cells were treated with increasing concentrations of heparinase III. At 1 h later, cells were transduced with RhAAV4282.eGFP. At 72 h later, GFP<sup>+</sup> cells were detected by flow cytometry. (B and C) CMAS (B) and (C) KIAA0319L KO cells were normalized to WT cells for RhAAV4282.eGFP transduction after 72 h. (D) Capsid stability of RhAAV4282, AAV7, and AAV9 was compared by incubating each capsid with SYPRO Orange dye and incrementally increasing temperature. The derivative signal/temperature was used to determine the  $T_m$  of the capsid. Separate biological replicates are denoted as black dots; black lines represent group medians. SEM for each temperature is denoted by colored horizontal lines in (D).

copies per diploid genome were calculated. The liver contained the largest amount of genome copies, as has been reported with other AAVs.<sup>31</sup> RhAAV4282 had modestly lower tropism for the liver than AAV7. Other tested tissues showed no statistically significant differences (Figure 4A). Since DNA localization can be unrelated to tissue transduction,<sup>31</sup> we tested RNA localization in the same tissues (Figure 4B). We found modestly higher RNA levels of AAV7 in liver than RhAAV4282. In other tissues, there were no differences observed. Surprisingly, we found that despite AAV9 DNA levels being lower than RhAAV4282 and AAV7 in the quadriceps, RNA measurement showed higher AAV9 RNA concentration compared to RhAAV4282 and AAV7 in the quadriceps. Protein localization was determined by IVIS signal (average radiance per second) (Figures 4C and 4D). Protein levels between RhAAV4282 and AAV7 repeated the same pattern observed in the RNA and DNA levels, with similar signals in all tissues tested except the liver, where AAV7 had more liver signal. AAV9 transduced quadriceps and diaphragm at a higher rate than RhAAV4282 and AAV7. Whole-mouse imaging confirmed that AAV9 transduced at a higher level than RhAAV4282 and AAV7 (Figure 4E).

#### Structural analysis of RhAAV4282

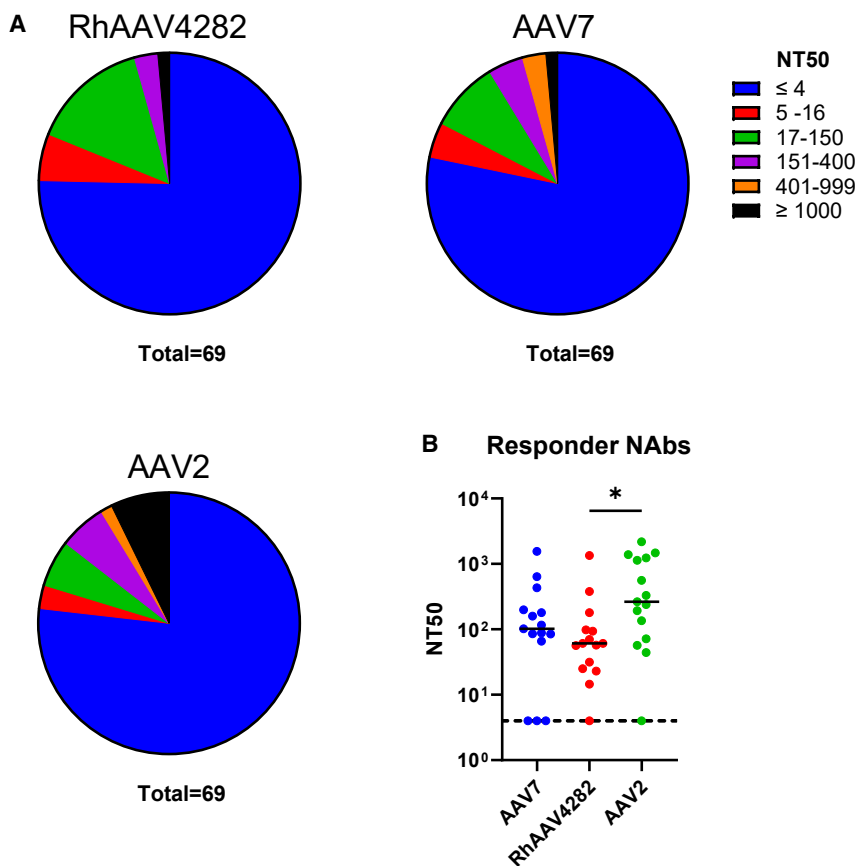
RhAAV4282 and AAV7 capsids share 91.4% sequence homology (Figure 1C), but showed differences in seroprevalence, liver tropism, and innate immune signaling. To evaluate the possible cause of these differences further, we determined a high-resolution cryo-EM structure of the RhAAV4282 capsid. A total of 69,220 RhAAV4282 particles were classified into empty (35,328; 51%) or full (33,892;

49%) particles from which we obtained two reconstructions and structural models for the RhAAV4282 capsid in either an empty or full configuration, respectively. The overall resolution of the empty capsid was 2.57 Å (Figure 5A). The overall resolution of the full capsid was 2.58 Å (Figure S10). As with previous AAV capsid structures, we did not resolve the N terminus of VP1 or VP2, and thus our model extends from amino acid 220 to 733 of the VP1 capsid sequence. The structures showed many common characteristics

of AAV capsids. These features include a 3-fold protrusion, a pore at the 5-fold axis, and valleys at the 2-fold axis.<sup>32</sup> Our models fit the electron density maps well, particularly for the core of the structure (Figure 5C). Somewhat poorer resolved density was observed in the outer loops of the capsid as expected due to increased flexibility of these segments (Figure 5D). We observed no substantial structural differences between the empty and full capsid maps (Figure S10), which is consistent with previously reported models of AAV capsids.<sup>33</sup>

Comparing the RhAAV4282 and AAV7 capsids revealed many structural similarities as expected, given the high level of sequence homology (Figure 5B). The largest structural difference corresponded to a 7-amino acid sequence difference that was located at the 3-fold proximal loop within hypervariable region IV<sup>34</sup> (Figure 5B, inset), where the AAV7 loop was longer and extended further into solution than the RhAAV4282 loop. This region also was different in the AAV9 capsid, which had a shorter loop than AAV7 but longer than RhAAV4282 (Figure S11).

Aligning the VP1 sequences of RhAAV4282 and AAV7 supports the results observed by cryoelectron microscopy (cryo-EM), with RhAAV4282 and AAV7 sharing a high degree of sequence similarity throughout VP1 (Figures 6A and 6B). Within the VP1 protein, only 65 amino acids differ between RhAAV4282 and AAV7. According to clustal omega, 47.7% (31/65) of these changes were changes between amino acids of strongly similar properties, 33.8% (22/65) of these amino acid changes are with amino acids that share weakly similar properties, and 18.5% (12/65) did not share properties or were

**Figure 3. Human seroprevalence**

Human serum samples from around the Boston area were measured for RhAAV4282, AAV7, and AAV2 NAb titers. (A) Responses were categorized for each virus. (B) All responders' (categorized as having NAb titers against RhAAV4282, AAV7, or AAV2) NAb titers plotted for each virus. Black bars represent medians.  $p$  values represent result of one-way ANOVA test. \* $p < 0.05$ .

administration of RhAAV4282.EGFP followed by RhAAV4282.Luc showed complete removal of luciferase signal presumably due to anti-vector immunity. In comparison, mice administered RhAAV4282.Luc following AAV7. EGFP injections showed systemic signal in 4/5 mice. Whole-mouse luminescence quantification showed that heterologous boosting resulted in at least a 1-log increase in signal compared to homologous boosting (Figure 7B).

#### HRNE modifications alter neutralization profiles for RhAAV4282 and AAV7

Some AAV gene therapies have shown that in certain disease settings, durability may be a concern, and booster shots could become necessary to maintain efficacy.<sup>16-18</sup> We sought to determine whether RhAAV4282 and AAV7 generated cross-NAbs and whether these NAb profiles could be altered by changing the HRNE. To test this hypothesis, we injected mice with 5E11 GC AAV7, RhAAV4282, and AAV9 encoding luciferase.

Our previous structure and sequence data also suggested that the HRNE could be a potential neutralization determinant if AAV7 and RhAAV4282 have different neutralization patterns. To test this hypothesis, we generated an AAV7 capsid with the RhAAV4282 HRNE (AAV7(4282L)) and a RhAAV4282 capsid with an AAV7 HRNE (RhAAV4282(AAV7L)). These mutants grew similarly to the parental strains. We included these mutants in our NAb tests at the same dose as the three wild-type (WT) vectors. Mouse tissue tropism was not substantially changed in the HRNE mutants (Figure S12). Mouse serum was collected 4 weeks after injection. We tested this serum for NAb against AAV7 (Figure 8A), RhAAV4282 (Figure 8B), and AAV9 (Figure 8C). We found that each vector primarily induced autologous neutralization with low heterologous neutralization (Figures 8A-8C), although a limited degree of cross-neutralization was observed for AAV7 and RhAAV4282 (Figures 8A and 8B).

We observed that swapping the seven amino acids constituting the HRNE resulted in modified NAb titers. Mice injected with AAV7 showed the highest NAb titers against AAV7 (median neutralizing titer [NT<sub>50</sub>]: 702.8) (Figure 8A), whereas mice injected

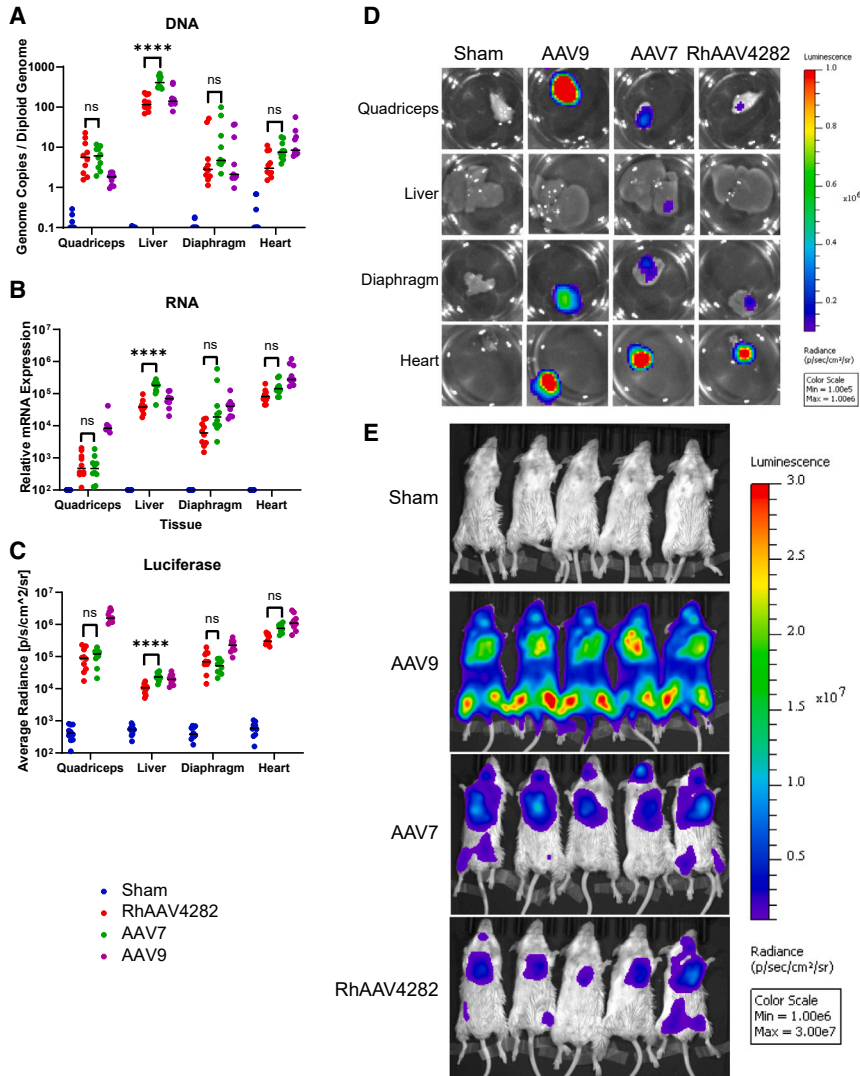
deletions. Seven amino acids that either shared weak similarities or no similarities, including a 3-amino acid deletion, were located between amino acids 453-460 of the AAV7 sequence. This is the same region identified by structural analysis near the 3-fold proximal peak contained within hypervariable region IV<sup>34</sup> (Figure 6C). We named this subregion the HRNE (denoted by black bracket in Figure 6D).

#### Mouse heterologous boost experiment

These results prompted us to evaluate whether AAV7 and RhAAV4282 would be useful for heterologous booster injections. To test this hypothesis, we injected mice with 5E11 genome copies (GC) of AAV7 or RhAAV4282 vectors encoding EGFP intravenously. Four weeks later, we administered 5E11 GC of either AAV7 or RhAAV4282 vectors encoding luciferase to each group and measured luminescence compared to mice receiving a single dose of AAV7 or RhAAV4282 encoding luciferase.

Whole-mouse imaging showed a high signal for mice having received single-shot AAV7 or RhAAV4282 expressing luciferase (Figure 7A). Mice injected with AAV7.EGFP followed by AAV7.Luc primarily showed signal at the site of administration (right eye) in 4/5 mice, presumably due to substantial suppression by anti-vector immunity induced by the initial inoculation. Homologous



**Figure 4. RhAAV4282 tissue tropism**

Mice were injected with 5E11 GC of AAVs expressing luciferase. Four weeks later, tissues were removed and used to measure (A) viral genome localization by qPCR, (B) viral transcript localization by RT-PCR, and (C) protein levels by measuring luminescence. (D) Representative image of tissues extracted from mice and immersed in PBS with luciferin. (E) Representative image of whole mouse luminescence after luciferin injection. Individual mice in (A)–(C) denoted as dots, with group median values denoted by black lines. *p* values represent result of one-way ANOVA test for each tissue for (A) DNA, (B) RNA, and (C) luciferase. \*\*\*\**p* < 0.0001. Significance comparisons with AAV9 not shown.

tion epitopes that result in the high neutralization against RhAAV4282 in mice.

## DISCUSSION

AAV vectors for gene therapy can be limited by preexisting immunity to the vector or immunity induced by previous treatments.<sup>1,9–12,29,30</sup> To address these concerns, we identified a panel of new AAV capsids from rhesus macaques.<sup>20</sup> We identified five novel AAV capsids and characterized RhAAV4282, which shares 91.4% sequence homology with AAV7. *In vitro* experiments demonstrated that RhAAV4282, like AAV7, does not use common AAV attachment factors (sialic acid, heparin sulfate, and galactose) for cellular entry. AAV7 and RhAAV4282 also shared nearly identical capsid stability. These *in vitro* results indicate that RhAAV4282 and AAV7 capsids are highly similar and may even share a currently unknown attachment factor. These vectors also showed similar *in vivo* tropisms, although

RhAAV4282 showed slightly diminished signal compared to AAV7. Nevertheless, these two vectors differed in innate immune responses and neutralization profiles. We determined a cryo-EM structure of RhAAV4282 at 2.57Å and identified a 7-amino acid region within hypervariable region IV that differed substantially. We first tested that heterologous boosting of RhAAV4282 and AAV7 was more successful than homologous boosting. We then generated mutant RhAAV4282 and AAV7 capsids with this region swapped and showed that this region, which we termed the HRNE, was a neutralization epitope for AAV7 and RhAAV4282. We speculate the HRNE may be more immunodominant in AAV7 due to its longer length compared to the shorter RhAAV4282 HRNE. RhAAV4282 may also have additional neutralization epitopes that account for its higher overall anti-vector immunity.

Recent studies<sup>35,36</sup> have shown both the promise and limitations of AAV vectors. These observations emphasize the importance of

with AAV7(4282L) (median NT<sub>50</sub>: 116.0) showed substantially decreased NAb titers against AAV7. RhAAV4282 (median NT<sub>50</sub>: 16.5)-injected mice showed low NAb titers against AAV7, but RhAAV4282(AAV7L) (median NT<sub>50</sub>: 240.5) induced substantially increased AAV7 NAbs compared with RhAAV4282. These data suggest that the HRNE is an important neutralizing determinant for AAV7.

Similarly, RhAAV4282 led to robust NAbs against RhAAV4282 (median NT<sub>50</sub>: 1567.0), and AAV7 (median NT<sub>50</sub>: 7.5) injection led to minimal NAbs against RhAAV4282 (Figure 8B). AAV7(4282L) (median NT<sub>50</sub>: 179.0) induced substantially increased NAbs to RhAAV4282 compared with AAV7. These data suggest that the HRNE is also a partial neutralization epitope for RhAAV4282. However, mice injected with RhAAV4282(AAV7L) (median NT<sub>50</sub>: 1618) and RhAAV4282 showed similar NAbs against the RhAAV4282 capsid, suggesting that RhAAV4282 may have multiple neutraliza-

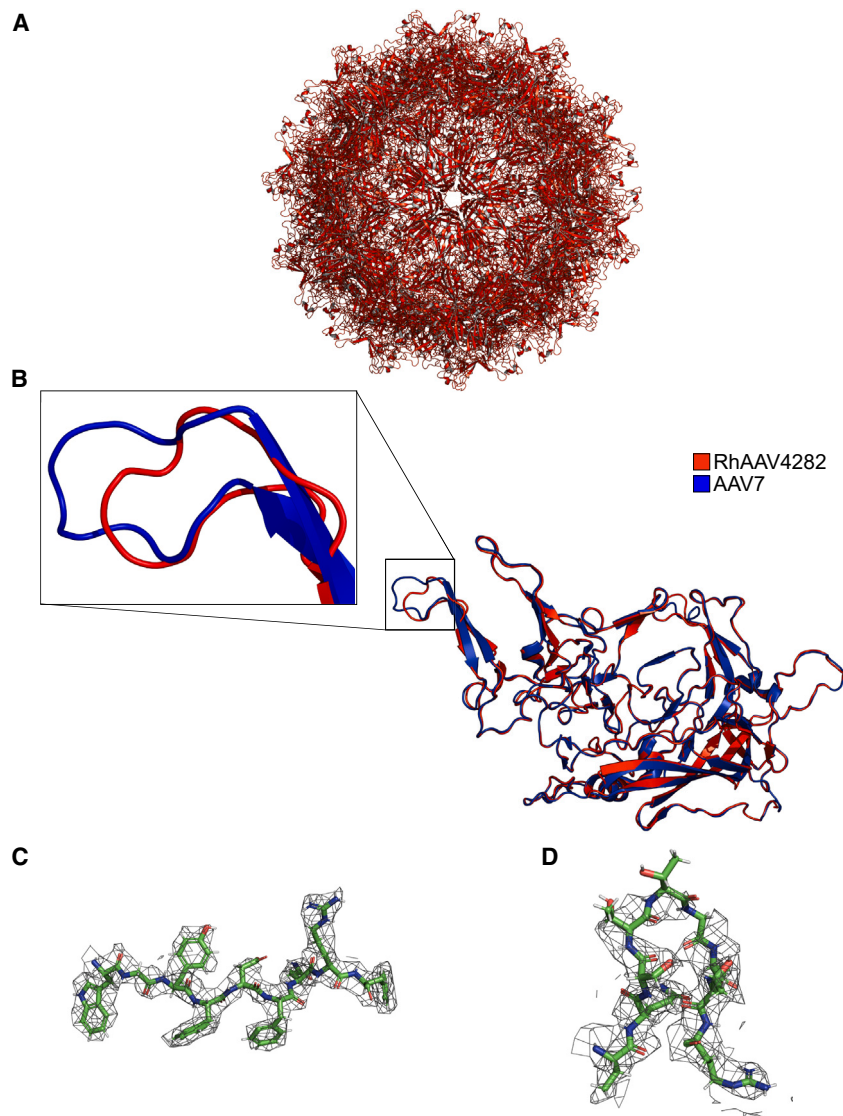


**Figure 5. Cryo-EM model of RhAAV4282 capsid**

(A) Atomic model from a cryo-EM reconstruction of the empty RhAAV4282 capsid to 2.57 Å resolution. (B) Structural comparison of RhAAV4282 VP3 monomer (red) aligned with an AAV7 VP3 monomer (blue) (7L5Q). Enlargement shows differences in the hypervariable region IV. RhAAV4282 electron density (gray mesh) and residues for one monomer of RhAAV4282 capsid (green) shown for amino acids (C) 280–288 and (D) 449–457 using RhAAV4282 VP1 amino acid numbering.

expanding the repertoire of AAV vectors both to further understand the biology of the vector and to increase the toolbox for gene therapy.<sup>37–39</sup> Previous studies have investigated swapping regions of the AAV capsid primarily to investigate tropism determinants,<sup>40,41</sup> although some studies have investigated immunogenicity determinants.<sup>34,42,43</sup> A few papers have identified the 3-fold spike region as an antigenic determinant, and the prominent AAV monoclonal antibody A20 has been shown to bind to this region along with other sites in AAV2.<sup>44–46</sup> Our study expands on this work and adds higher resolution by identifying the HRNE region in which just seven amino acids represent a major neutralization determinant for these two rhesus AAVs.

In some cases, gene therapies may not be durable for the lifetime of the patient, necessitating repeat treatments.<sup>16–19</sup> Unfortunately, it is rarely possible to give the same treatment due to the generation of NAb

against the original treatment AAV capsid.<sup>47</sup> This presents three options: excluding patients,<sup>14</sup> immunosuppressing patients,<sup>48</sup> or utilizing an alternative AAV capsid with a different neutralization profile. Modifications to the HRNE or loop-swap mutants could provide an alternative to these options and may allow more efficient sequential dosing.

In conclusion, we identified five novel AAV capsids from rhesus macaques and characterized RhAAV4282 biochemically and structurally. Utilizing the cryo-EM structure, we used mutant vectors to identify the HRNE as a neutralization determinant for these AAVs. This work will enable future research into the immune response to AAV capsids and could allow the development of immune evasion strategies for AAV vectors.

## MATERIALS AND METHODS

### Isolation and vectorization of novel rhesus macaque AAVs

Stool samples from rhesus macaques (*M. mulatta*), which tested positive for the presence of AAV by metagenomics sequencing,<sup>20</sup> were resuspended in unsupplemented DMEM and filtered through a 0.45- $\mu$ m pore-size filter. Human E1-complementing cells were infected with the filtrates, incubated at 37°C with 10% CO<sub>2</sub>, and monitored for CPES.<sup>49</sup> DNA was extracted from infected cell supernatants and subjected to PCR amplification using degenerate primers targeting the Cap gene of AAV. Primers were designed to an alignment of readily available Cap genes from the GenBank database. PCR fragments were analyzed on agarose gel, and those of the expected size were extracted and cloned into an in-house constructed AAV2 RepCap plasmid, using Gibson assembly.<sup>50</sup> Isolated Cap genes were verified to be novel by blasting on GenBank. Recombinant AAV was rescued by transfecting human embryonic kidney cells by triple transfection together with an in-house-generated AAV2 inverted terminal repeat (ITR) plasmid, carrying a transgene expression cassette consisting of a cytomegalovirus (CMV) promoter, a multiple-cloning site, and a simian virus 40 polyadenylation signal, together with a helper plasmid

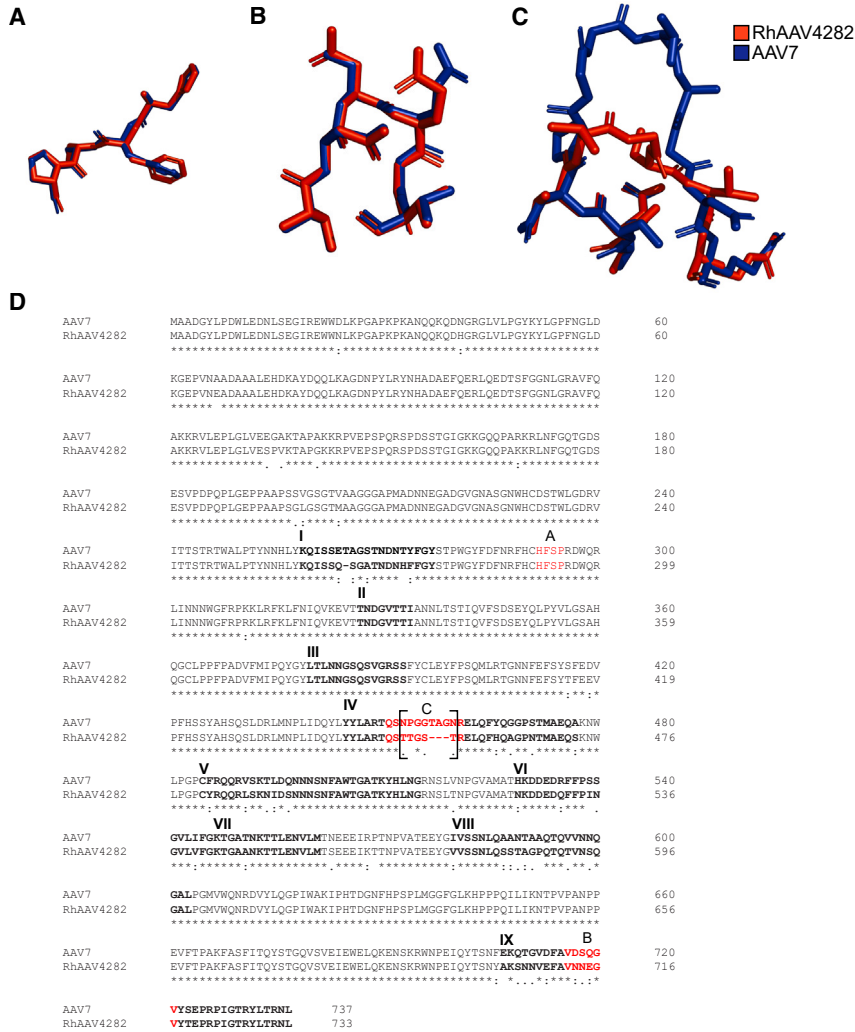


**Figure 6. Sequence and structural comparison to AAV7**

(A–C) Structural alignment of RhAAV4282 capsid amino acids (A) 292–295, (B) 715–720, and (C) 451–461 (using AAV7 amino acid numbering). (D) Sequence alignment of RhAAV4282 and AAV7 VP1 amino acid sequence. Hypervariable regions are numbered (I–IX) and denoted by bold letters. Sequences displayed in (A)–(C) are shown by red lettering. HRNE is designated by black brackets. “\*” signifies an exact match of amino acids; “.” signifies an amino acid change of amino acids with strongly similar properties; “.” denotes an amino acid change of amino acids with weakly similar properties; “” denotes a swap of amino acids that share no similar properties or a deletion.

AAV9.Luc used in animal studies was purchased from Vigene Biosciences as a custom order using the same AAV2.ITR transgene cassette packaged into AAV7 and novel rhesus AAVs. AAV9.Luc used in neutralization assay studies was grown and purified as previously described, in the same way as all other vectors.

## Cryo-EM

### Specimen preparation and cryo-EM data collection

Purified RhAAV4282.eGFP (3.5  $\mu$ L) [2.1E13 GC/mL] was applied onto a glow-discharged, 400-mesh copper Quantifoil R1.2/1.3 holey carbon grid (Quantifoil). Grids were blotted for 7 s at  $\sim$ 80% humidity and flash-frozen by liquid nitrogen-cooled liquid ethane using an FEI Vitrobot Mark I (FEI). The grid was then loaded onto an FEI TF30 Polara

electron microscope operating at 300-kV accelerating voltage. Image stacks were recorded on a Gatan K2 Summit (Gatan) direct detector set in counting mode with gain-reference correction applied using SerialEM,<sup>52</sup> with a defocus range between 1.5 and 3.0  $\mu$ m. The electron dose was set to 8 e<sup>-</sup>/physical pixel/s, and the sub-frame time was set to 200 ms. A total exposure time of 10 s resulted in 50 sub-frames per image stack. The total electron dose was 52.8 e<sup>-</sup>/Å<sup>2</sup> ( $\sim$ 1.1 e<sup>-</sup>/Å<sup>2</sup> per sub-frame).

### Cryo-EM data processing

We aligned the frames from 4,525 movies using MotionCor2<sup>53</sup> with 5  $\times$  5 patch alignment to calculate summed micrographs. We used the template-matching routines from cisTEM (match\_template, version 1.00; refine\_template, version 1.00; make\_template\_result, version 1.00) to pick 69,365 virus particles from the summed micrographs.<sup>54,55</sup> Matching was done at 5-Å resolution with 2 $\times$  binned micrographs, 1.43 $^\circ$  initial angular sampling, and a template

carrying adenovirus helper genes E2, E4 and VA RNA. Virus was purified through iodixanol density centrifugation through standard protocols.<sup>51</sup>

## AAV growth and purification

A transgene cassette containing a CMV promoter and the transgene of interest (e.g., luciferase, EGFP) was cloned into an AAV2.ITR plasmid. The AAV2.ITR plasmid was co-transfected with the Rep/Cap plasmid and a pHelper plasmid (Applied Viro-mics) into 293T/17 cells plated 1 day prior to transfection. Cells were incubated at 37 $^\circ$ C with 10% CO<sub>2</sub>. After 72 h, cell supernatant was harvested and combined with 5 $\times$  polyethylene glycol solution (Teknova, catalog no. P4190) and incubated at 4 $^\circ$ C overnight. Supernatant was then centrifuged at 8,000  $\times$  g for 30 min to pellet the virus. Pellets were resuspended and treated with benzonase. Virus was purified using iodixanol gradient centrifugation. Packaged virus particles were quantified by qPCR using primers targeting the CMV promoter region.



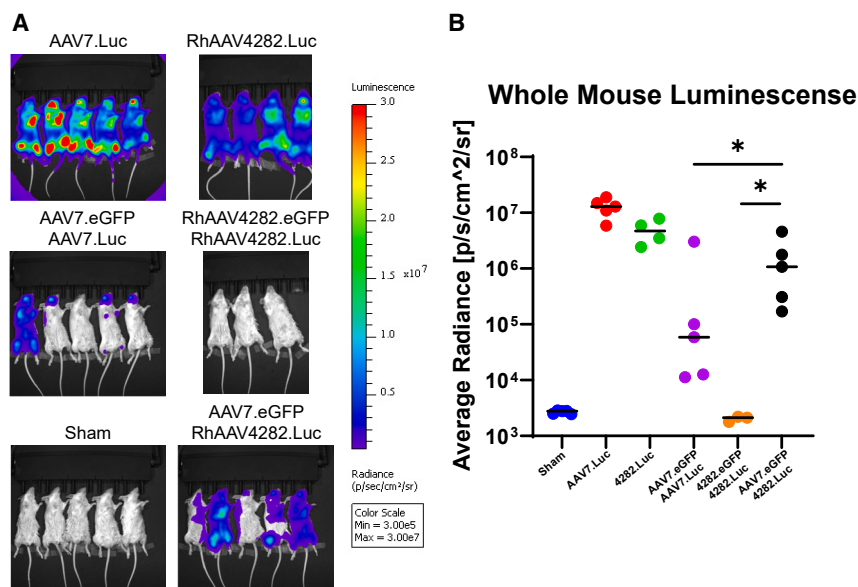


**Figure 7. Heterologous mouse boost**

Mice were injected with 5E11 GC of AAVs expressing EGFP. Four weeks later, mice were injected with 5E11 GC of AAVs expressing luciferase in either a homologous or heterologous dose. (A) Four weeks post-boost, whole-mouse imaging was conducted to determine the success of AAVs expressing luciferase. (B) Whole-mouse signal was quantified with regions of interest covering each mouse body, excluding the head. Individual mice denoted as separate dots. Black bars represent group medians.  $p$  values represent result of one-way Mann-Whitney test. \* $p < 0.05$ .

reference obtained from cryoSPARC with an  $I_1$  icosahedral symmetry setting.<sup>56</sup> With GPU-accelerated computer program Gctf,<sup>57</sup> we estimated contrast transfer function (CTF) parameters from the total summed micrographs with local refinement at particle positions. We used *reliion\_preprocess*<sup>58</sup> for particle extraction and normalization (box size of  $384 \times 384$  pixels). After two-dimensional classification with *reliion\_refine*,<sup>58</sup> we retained 69,220 particles for subsequent analysis. To obtain the best icosahedral reconstructions, we used *cisTEM*<sup>54</sup> (*refine3D* version 1.01, *reconstruct3D* version 1.02) with  $I_1$  symmetry imposed for particle alignment and classification (sorting full and empty particles, see below), *reliion\_motion\_refine*, and *reliion\_ctf\_refine*<sup>59</sup> in two iterations. The spherical shell mask that we used for the calculations had an inner radius of 74 Å and an outer radius of 150 Å. The alignment resolution in the last step was 3.4 Å, and *reliion\_ctf\_refine* was run with the following input options: `-fit_defocus -kmin_defocus 30 -fit_mode fpmfp -fit_beamtilt -kmin_tilt 30 -fit_aniso -odd_aberr_max_n 3 -fit_aberr`. We reconstructed maps with *reliion\_reconstruct* with the option `-fom_weighting`, where we assigned per-particle figure of merits (*FOM*) based on the *cisTEM* alignment score, where  $S_i$  is the score of particle  $i$ , and  $S_{max}$  and  $S_{min}$  are the highest and lowest scores, respectively:

$$FOM = \frac{S_i - S_{min}}{S_{max} - S_{min}} \quad (\text{Equation 1})$$

For a map calculated with the full particle stack, the Fourier shell correlation (FSC) calculated from half-map densities within the volume of the spherical shell mask dropped below 0.143 at a spatial frequency corresponding to 2.49 Å (which was almost Nyquist frequency given a pixel size of 1.23 Å) (Table S2). To separate empty from full viral particles, we used three-dimensional (3D) classification in *cisTEM*<sup>60</sup> with a spherical mask (inner radius of

0 Å and an outer radius of 150 Å). This yielded two image stacks, with 35,328 empty particles (51%) and 33,892 full particles (49%). The reconstructions calculated from these two stacks had a nominal resolution of 2.57 and 2.58 Å, respectively (Table S2). FSC curves from masked half-maps were calculated with *phenix.mtriage*,<sup>61</sup> and local resolutions were estimated with *reliion\_postprocess*. Maps were sharpened with *sharpen\_map* from *cisTEM*.<sup>54</sup>

#### Model building and refinement

We obtained a predicted dimer structure of two RhAAV4282 protomers from AlphaFold 2,<sup>62</sup> from which we then placed one protomer into the density map, refined the protomer structure, followed this with expansion to generate the viral capsid by applying icosahedral symmetry and refinement of the capsid. After an initial round of refinement with *phenix.real\_space\_refine*,<sup>63</sup> we manually checked the models in *O*<sup>64</sup> and *Coot*,<sup>65</sup> and made a few minor adjustments where necessary. We performed the final structure refinement with global minimization, local grid searches, and *B* factor adjustment, and with a target function that contained standard stereochemical and *B* factor restraints, rotamer and Ramachandran restraints, secondary structure restraints, and non-crystallographic symmetry constraints.<sup>63</sup> Modeled residues for the empty and full capsids are listed in Table S2. We probed the stereochemistry of the structures with *MolProbity*<sup>66</sup> (Table S2).

#### Figure preparation

We prepared the figures using *PyMOL* version 2.3 (Schrödinger) and *matplotlib*.<sup>67</sup>

#### Density maps and atomic coordinates accession identifiers

The cryo-EM maps can be obtained from the Electron Microscopy DataBank (EMD-44197, empty viral capsid; EMD-44196, full viral capsid) and the atomic coordinates from PDB (PDB: 9B53, empty viral capsid; PDB: 9B52, full viral capsid).

#### AAV NAb assay

The AAV NAb assay was adapted from Krotova and Aslanidi (2020).<sup>68</sup> Serum was heat inactivated for 30 min at 56°C. The 293T

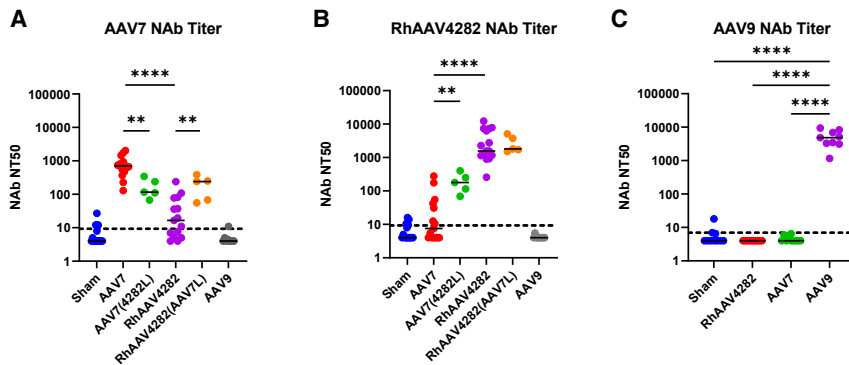


**Figure 8. NAb titers**

HRNE region can significantly change NAb titers between AAV7 and RhAAV4282. Mice were injected with 5E11 GC of AAVs. Four weeks post-injection, serum was collected from mice and tested for NAb titers. Mouse groups are shown on the x axis (A–C). Serum was tested against (A) AAV7, (B) RhAAV4282, and (C) AAV9 in an AAV neutralization assay. Individual mice in (A)–(C) denoted as dots, with group median values denoted by black lines.  $p$  values represent results of one-way ANOVA tests for NAb against each virus. \* $p < 0.05$ ; \*\* $p < 0.01$ ; \*\*\* $p < 0.001$ ; \*\*\*\* $p < 0.0001$ . Limit of quantification was defined as 2 SDs from the mean for sham in each plot and is denoted by black dotted line.

cells were seeded in 96-well plates at 20,000 cells per well and then incubated overnight. The next day, the serum for testing was serially diluted either 2-fold or 4-fold. 15  $\mu$ L of 3.13E9 GC/mL of the appropriate AAV vector was mixed with serially diluted serum in a 1:1 or 1:3 ratio, and this mixture was incubated at 37°C for 1 h. During this incubation, cells were incubated with 20  $\mu$ M dorsomorphin (Abcam, catalog no. ab120843) at 37°C for 1 h. After incubation, 10  $\mu$ L AAV vector and serum mixture was added to the cells (still containing dorsomorphin) to a final concentration of 9.77E7 GC per well. Cells were incubated for 48 h at 37°C. After incubation, cells were lysed in Steady-Glo luciferase assay (Promega) according to the manufacturer's instructions. AAV neutralization titers were defined as the sample dilution at which a 50% reduction in luciferase signal is observed relative to the average of the virus control wells.

#### DNA and RNA extraction from tissues

qRT-PCR and qPCR assays were used as previously described.<sup>69</sup> Briefly, RNA was extracted from tissues using a Qiacube HT (Qiagen, Germany) and the RNeasy 96 QIacube HT kit. DNA was extracted from tissues using a Qiacube HT (Qiagen) and the QIAamp 96 QIacube HT kit. Two samples from each tissue were removed and placed in separate 2-mL Eppendorf tubes containing a 5-mm stainless-steel bead and either 700  $\mu$ L QIAzol lysis buffer or 450  $\mu$ L ATL buffer + Proteinase K for RNA and DNA extraction, respectively. RNA extraction tubes were shaken twice at 25 Hz for 5 min using the Qiagen TissueLyser II. Following lysis, 200  $\mu$ L chloroform was added and manually shaken. Samples were then incubated for 3 min at room temperature and centrifuged for 15 min at 4°C. Following centrifugation, the aqueous phase was transferred to a deep-well 96-well plate, and total RNA was isolated using the QIacube HT system. For the DNA extraction, tissue tubes were shaken twice for 1 min at 25 Hz in the Qiagen TissueLyser II. Afterward, 50  $\mu$ L Proteinase K was added to the samples and incubated at 56°C with shaking overnight. Genomic DNA was then extracted using the Qiacube HT system.

RNA was reverse transcribed using superscript VILO (Invitrogen) and run in duplicate using the Quantstudio 6 and 7 Flex Real-Time PCR System (Applied Biosciences) according to the manufacturer's instructions. The RNA concentration was calculated using the  $2^{-\Delta\Delta CT}$

method<sup>70</sup> using glyceraldehyde 3-phosphate dehydrogenase as a housekeeping gene (Thermo Fisher, catalog no. 4352339E) and luciferase as the gene of interest (Thermo Fisher, catalog no. 4351370). The DNA concentration was determined using primers targeting the CMV promoter region of the AAV vector transgene (forward: TGCCCACTTGGCAGTACATCA, reverse: GCCAAGTAGGAAAGTCCATAAGGT, probe: TGGCCCGCTGGCATTATGCCAGT) and normalizing using the Tfic kit (Thermo Fisher, catalog no. 4458367). Genome copies per diploid genome were determined using CopyCaller Software version 2.1 software (Thermo Fisher Scientific) according to the manufacturer's instructions.

#### IVIS imaging

To image luciferase expression, mice were injected with 150  $\mu$ L luciferin (IVISbrite D-Luciferin Ultra Bioluminescent Substrate in Rediject Solution, PerkinElmer, catalog no. 770505) through the intraperitoneal route. Mice were then kept awake for 6 min, after which mice were anesthetized using isoflurane for 3 min. Mice were then imaged in the IVIS Lumina LT Instrument Series III for 3 min for whole-mouse images. For tissue signal, mice were administered luciferin as previously described for whole-mouse imaging, but after 3 min under isoflurane, mice were euthanized with CO<sub>2</sub>. Tissues of interest were then harvested, briefly washed in PBS, then placed into 6-well plates filled with 3 mL PBS mixed with 75  $\mu$ L luciferin. Tissues were imaged for 3 min. Afterward tissues were placed into RNeasy lysis buffer (Qiagen, catalog no. 70610) solution for later DNA and RNA extraction.

#### In vitro receptor assays

AAVR-KO and H1 HeLa WT control cells were a generous gift from Jan Carette at Stanford University. CMAS-KO with WT HEK293T control cells were purchased as a custom order from Canopy Biosciences (catalog no. KOCE-V2-0012426). HeLa cells were purchased from Canopy Biosciences. AC16 cells were purchased from Sigma Aldrich (SCC109). A549 (catalog no. CCL-185) and HepG2 (catalog no. HB-8065) cells were obtained from American Type Culture Collection. All cells except AC16 cells were grown in DMEM with 10% fetal bovine serum (FBS) and 1% MgCl<sub>2</sub>. AC16 cells were grown in DMEM:F12 (Thermo Fisher) with 12.5% FBS, 2 nM glutamine, and

1% penicillin-streptomycin. Cells were seeded in a 96-well plate at 10,000 cells per well. After overnight incubation, AAV vectors encoding EGFP were added at the following MOIs: 0, 1,000, 5,000, 10,000, 50,000, and 100,000. After 72 h (or 24 h in the case of [Figures S3 and S4](#)) cells were harvested and stained with LIVE/DEAD stain (Thermo Fisher Scientific, catalog no. L34976) and fixed with paraformaldehyde. Flow cytometry was then used to quantify the percentage of live cells that were GFP<sup>+</sup>. For each vector, the MOI was selected as the lowest MOI where a majority of WT cells were GFP<sup>+</sup>. If no MOI reached over 50%, the highest MOI was used. GFP positivity was used as a surrogate for successful infection.

For heparin attachment factor testing, 293T cells were plated as previously described for KO experiments. After overnight incubation, cells were incubated with successive dilutions of heparinase III from *Flavobacterium heparinum* (Sigma-Aldrich, catalog no. H8891-10UN) for 1 h at room temperature. Cells were washed with PBS. Then, AAV vectors encoding EGFP were added at the following MOIs per serotype: AAV1: 10,000 MOI, AAV2: 1,000 MOI, AAV9: 100,000 MOI, and RhAAV4282: 100,000 MOI. After 72 h, cells were harvested and stained with LIVE/DEAD stain (Thermo Fisher Scientific) and fixed with paraformaldehyde. Flow cytometry was then used to quantify the percentage of live cells that were GFP<sup>+</sup>.

#### Capsid stability assay

SYPRO Orange (Thermo Fisher, catalog no. S6651) was diluted 1:100 in PBS. SYPRO Orange (2.5  $\mu$ L), AAV of interest (5  $\mu$ L), and 17.5  $\mu$ L Dulbecco's PBS were combined. Sample fluorescence readings was monitored using a Quantstudio 6 and 7 Flex Real-Time PCR System (Applied Biosciences). Samples were incubated at 25°C for 2 min. Then, a temperature gradient from 25°C to 99°C was conducted at 0.05°C per step.

#### Mice

Female 6- to 10-week-old BALB/c mice (The Jackson Laboratory) were randomly allocated to groups. Mice received AAV administrations as 5E11 GC through retro-orbital injection. Peripheral blood was collected through submandibular bleeds to isolate serum for immunological assays. All animal studies were conducted in compliance with all relevant local, state, and federal regulations and were approved by the Beth Israel Deaconess Medical Center Institutional Animal Care and Use Committees.

#### Innate immune cytokine analysis

Concentration of 19 cytokines was measured using the V-PLEX Plus Mouse Cytokine 19-Plex Kit (catalog no. K15255G-1) from Meso Scale Discovery. The lower limit of detection for each cytokine is as follows: IFN- $\gamma$  (0.04 pg/mL), IL-1 $\beta$  (0.11 pg/mL), IL-5 (0.06 pg/mL), IL-6 (0.61 pg/mL), IL-10 (0.94 pg/mL), IP-10 (0.328 pg/mL), keratinocyte chemoattractant/human growth-regulated oncogene (0.24 pg/mL), MCP-1 (0.672 pg/mL), macrophage inflammatory protein-1 $\alpha$  (MIP-1 $\alpha$ ; 0.081 pg/mL), MIP-2 (0.053 pg/mL), and tumor necrosis factor  $\alpha$  (0.13 pg/mL). Samples were run in singlets. The assay was conducted by the Metabolism and Mitochondrial Research Core (Beth Israel

Deaconess Medical Center, Boston, MA) following the manufacturer's instruction. Assay plates were read by a Meso QuickPlex SQ120 instrument, and the data were analyzed using Discovery Workbench 4.0 software.

#### Human samples

Cryopreserved, deidentified samples from 2020 to 2021 were utilized for testing NAb titers against RhAAV4282 and AAV7. The Beth Israel Deaconess Medical Center institutional review board approved the biorepository study and the parent biorepository study. All participants provided informed consent.

#### DATA AND CODE AVAILABILITY

All data are available in the manuscript or the supplemental information. The cryo-EM maps can be obtained from the Electron Microscopy DataBank (EMD: 44197, empty viral capsid; EMD: 44196, full viral capsid) and the atomic coordinates from the PDB (PDB: 9B53, empty viral capsid; PDB: 9B52, full viral capsid). AAV capsid sequences are available at GenBank under the following accession numbers GenBank: PQ140581–PQ140587.

#### ACKNOWLEDGMENTS

We acknowledge support from the National Institutes of Health (OD011170 and AI128751), the Massachusetts Consortium for Pathogen Readiness, and the Ragon Institute (to D.H.B.). We also acknowledge the Harvard Medical School Structural Biology Core.

#### AUTHOR CONTRIBUTIONS

This study was designed by G.D. and D.H.B. Vector cloning was performed by G.D., L.J.T., P.A., and D.H.B. Immunologic and virologic assays were performed by G.D., J.L.F., D.L., and Z.L. Structural studies were performed by G.D., S.J., and Z.L. The paper was written by G.D., D.H.B., and all co-authors.

#### DECLARATION OF INTERESTS

The authors declare no competing interests.

#### SUPPLEMENTAL INFORMATION

Supplemental information can be found online at <https://doi.org/10.1016/j.omtm.2024.101350>.

#### REFERENCES

- Calcedo, R., and Wilson, J.M. (2013). Humoral Immune Response to AAV. *Front. Immunol.* 4, 341. <https://doi.org/10.3389/fimmu.2013.00341>.
- Rivera, V.M., Gao, G.-p., Grant, R.L., Schnell, M.A., Zoltick, P.W., Rozamus, L.W., Clackson, T., and Wilson, J.M. (2005). Long-term pharmacologically regulated expression of erythropoietin in primates following AAV-mediated gene transfer. *Blood* 105, 1424–1430. <https://doi.org/10.1182/blood-2004-06-2501>.
- Sabatino, D.E., Lange, A.M., Altynova, E.S., Sarkar, R., Zhou, S., Merricks, E.P., Franck, H.G., Nichols, T.C., Arruda, V.R., and Kazanian, H.H., Jr. (2011). Efficacy and Safety of Long-term Prophylaxis in Severe Hemophilia A Dogs Following Liver Gene Therapy Using AAV Vectors. *Mol. Ther.* 19, 442–449. <https://doi.org/10.1038/mt.2010.240>.
- Rabinowitz, J.E., and Samulski, R.J. (2000). Building a better vector: the manipulation of AAV virions. *Virology* 278, 301–308.
- Korneyenkov, M.A., and Zamyatnin, A.A. (2021). Next Step in Gene Delivery: Modern Approaches and Further Perspectives of AAV Tropism Modification. *Pharmaceutics* 13, 750.
- Srivastava, A., and Carter, B.J. (2017). AAV Infection: Protection from Cancer. *Hum. Gene Ther.* 28, 323–327. <https://doi.org/10.1089/hum.2016.147>.

7. Kuzmin, D.A., Johnston, N.R., Smith, O.P., Fedorin, V.V., Kukushkin, Y.S., van der Loo, J.C.M., and Johnstone, E.C. (2021). The clinical landscape for AAV gene therapies. *Nat. Rev. Drug Discov.* 20, 173.
8. Duan, D. (2023). Mini-review: Lethal immunotoxicity in high-dose systemic AAV therapy. *Mol. Ther.* 31, 3123–3126. <https://doi.org/10.1016/j.ymthe.2023.10.015>.
9. Hurlbut, G.D., Ziegler, R.J., Nietupski, J.B., Foley, J.W., Woodworth, L.A., Meyers, E., Bercury, S.D., Pande, N.N., Souza, D.W., Bree, M.P., et al. (2010). Preexisting Immunity and Low Expression in Primates Highlight Translational Challenges for Liver-directed AAV8-mediated Gene Therapy. *Mol. Ther.* 18, 1983–1994. <https://doi.org/10.1038/mt.2010.175>.
10. Scallan, C.D., Jiang, H., Liu, T., Patarroyo-White, S., Sommer, J.M., Zhou, S., Couto, L.B., and Pierce, G.F. (2006). Human immunoglobulin inhibits liver transduction by AAV vectors at low AAV2 neutralizing titers in SCID mice. *Blood* 107, 1810–1817. <https://doi.org/10.1182/blood-2005-08-3229>.
11. Wang, L., Calcedo, R., Wang, H., Bell, P., Grant, R., Vandenberghe, L.H., Sanmiguel, J., Morizono, H., Batshaw, M.L., and Wilson, J.M. (2010). The Pleiotropic Effects of Natural AAV Infections on Liver-directed Gene Transfer in Macaques. *Mol. Ther.* 18, 126–134. <https://doi.org/10.1038/mt.2009.245>.
12. Boutin, S., Monteilh, V., Veron, P., Leborgne, C., Benveniste, O., Montus, M.F., and Masurier, C. (2010). Prevalence of Serum IgG and Neutralizing Factors Against Adeno-Associated Virus (AAV) Types 1, 2, 5, 6, 8, and 9 in the Healthy Population: Implications for Gene Therapy Using AAV Vectors. *Hum. Gene Ther.* 21, 704–712. <https://doi.org/10.1089/hum.2009.182>.
13. Fitzpatrick, Z., Leborgne, C., Barbon, E., Masat, E., Ronzitti, G., van Wittenbergh, L., Vignaud, A., Collaud, F., Charles, S., Simon Sola, M., et al. (2018). Influence of Pre-existing Anti-capsid Neutralizing and Binding Antibodies on AAV Vector Transduction. *Mol. Ther. Methods Clin. Dev.* 9, 119–129. <https://doi.org/10.1016/j.omtm.2018.02.003>.
14. Earley, J., Piletska, E., Ronzitti, G., and Piletsky, S. (2023). Evading and overcoming AAV neutralization in gene therapy. *Trends Biotechnol.* 41, 836–845. <https://doi.org/10.1016/j.tibtech.2022.11.006>.
15. Ertl, H.C.J. (2022). Immunogenicity and toxicity of AAV gene therapy. *Front. Immunol.* 13, 975803. <https://doi.org/10.3389/fimmu.2022.975803>.
16. Kaiser, J. (2023). Gene therapy milestone looms, but field seeks better options. *Science (New York, N.Y.)* 380, 778–779.
17. Shen, W., Liu, S., and Ou, L. (2022). rAAV immunogenicity, toxicity, and durability in 255 clinical trials: A meta-analysis. *Front. Immunol.* 13, 1001263. <https://doi.org/10.3389/fimmu.2022.1001263>.
18. Muhuri, M., Levy, D.L., Schulz, M., McCarty, D., and Gao, G. (2022). Durability of transgene expression after rAAV gene therapy. *Mol. Ther.* 30, 1364–1380.
19. Kuzmin, D.A., Shutova, M.V., Johnston, N.R., Smith, O.P., Fedorin, V.V., Kukushkin, Y.S., van der Loo, J.C.M., and Johnstone, E.C. (2021). The clinical landscape for AAV gene therapies. *Nat. Rev. Drug Discov.* 20, 173–174.
20. Handley, S.A., Thackray, L.B., Zhao, G., Presti, R., Miller, A.D., Droit, L., Abbink, P., Maxfield, L.F., Kambal, A., Duan, E., et al. (2012). Pathogenic Simian Immunodeficiency Virus Infection Is Associated with Expansion of the Enteric Virome. *Cell* 151, 253–266. <https://doi.org/10.1016/j.cell.2012.09.024>.
21. Pillay, S., Meyer, N.L., Puschnik, A.S., Davulcu, O., Diep, J., Ishikawa, Y., Jae, L.T., Wosen, J.E., Nagamine, C.M., Chapman, M.S., and Carette, J.E. (2016). An essential receptor for adeno-associated virus infection. *Nature* 530, 108–112. <https://doi.org/10.1038/nature16465>.
22. Pillay, S., Zou, W., Cheng, F., Puschnik, A.S., Meyer, N.L., Ganaie, S.S., Deng, X., Wosen, J.E., Davulcu, O., Yan, Z., et al. (2017). Adeno-associated Virus (AAV) Serotypes Have Distinctive Interactions with Domains of the Cellular AAV Receptor. *J. Virol.* 91, e00391-17. <https://doi.org/10.1128/jvi.00391-00317>.
23. Cornelissen, L.A.M., Blanas, A., van der Horst, J.C., Kruijssen, L., Zaal, A., O'Toole, T., Wiercx, L., van Kooyk, Y., and van Vliet, S.J. (2019). Disruption of sialic acid metabolism drives tumor growth by augmenting CD8+ T cell apoptosis. *Int. J. Cancer* 144, 2290–2302. <https://doi.org/10.1002/ijc.32084>.
24. Liu, Y., Sheng, J., Baggen, J., Meng, G., Xiao, C., Thibaut, H.J., van Kuppeveld, F.J.M., and Rossmann, M.G. (2015). Sialic acid-dependent cell entry of human enterovirus D68. *Nat. Commun.* 6, 8865. <https://doi.org/10.1038/ncomms9865>.
25. Bell, C.L., Vandenberghe, L.H., Bell, P., Limberis, M.P., Gao, G.-P., Van Vliet, K., Agbandje-McKenna, M., and Wilson, J.M. (2011). The AAV9 receptor and its modification to improve in vivo lung gene transfer in mice. *J. Clin. Invest.* 121, 2427–2435. <https://doi.org/10.1172/JCI57367>.
26. Huang, L.-Y., Patel, A., Ng, R., Miller, E.B., Halder, S., McKenna, R., Asokan, A., and Agbandje-McKenna, M. (2016). Characterization of the Adeno-Associated Virus 1 and 6 Sialic Acid Binding Site. *J. Virol.* 90, 5219–5230. <https://doi.org/10.1128/jvi.00161-16>.
27. Bell, C.L., Gurda, B.L., Van Vliet, K., Agbandje-McKenna, M., and Wilson, J.M. (2012). Identification of the Galactose Binding Domain of the Adeno-Associated Virus Serotype 9 Capsid. *J. Virol.* 86, 7326–7333. <https://doi.org/10.1128/jvi.00448-12>.
28. Chowdhury, E.A., Meno-Tetang, G., Chang, H.Y., Wu, S., Huang, H.W., Jamier, T., Chandran, J., and Shah, D.K. (2021). Current progress and limitations of AAV mediated delivery of protein therapeutic genes and the importance of developing quantitative pharmacokinetic/pharmacodynamic (PK/PD) models. *Adv. Drug Deliv. Rev.* 170, 214–237. <https://doi.org/10.1016/j.addr.2021.01.017>.
29. Wei, C., Li, D., Zhang, M., Zhao, Y., Liu, Y., Fan, Y., Wang, L., Liu, J., Chang, X., Jiang, Y., and Xiong, H. (2024). Prevalence of Adeno-Associated Virus-9 Neutralizing Antibody in Chinese Patients with Duchenne Muscular Dystrophy. *Hum. Gene Ther.* 35, 26–35. <https://doi.org/10.1089/hum.2023.117>.
30. Weber, T. (2021). Anti-AAV Antibodies in AAV Gene Therapy: Current Challenges and Possible Solutions. *Front. Immunol.* 12, 658399. <https://doi.org/10.3389/fimmu.2021.658399>.
31. Tabebordbar, M., Lagerborg, K.A., Stanton, A., King, E.M., Ye, S., Tellez, L., Krunnusz, A., Tavakoli, S., Widrick, J.J., Messmer, K.A., et al. (2021). Directed evolution of a family of AAV capsid variants enabling potent muscle-directed gene delivery across species. *Cell* 184, 4919–4938.e22.
32. Agbandje-McKenna, M., and Kleinschmidt, J. (2011). AAV capsid structure and cell interactions. *Methods Mol. Biol.* 807, 47–92.
33. Mietzsch, M., Barnes, C., Hull, J.A., Chipman, P., Xie, J., Bhattacharya, N., Sousa, D., McKenna, R., Gao, G., and Agbandje-McKenna, M. (2020). Comparative Analysis of the Capsid Structures of AAVrh.10, AAVrh.39, and AAV8. *J. Virol.* 94, e01769-19. <https://doi.org/10.1128/jvi.01769-01719>.
34. Mays, L.E., Wang, L., Tenney, R., Bell, P., Nam, H.-J., Lin, J., Gurda, B., Van Vliet, K., Mikals, K., Agbandje-McKenna, M., and Wilson, J.M. (2013). Mapping the Structural Determinants Responsible for Enhanced T Cell Activation to the Immunogenic Adeno-Associated Virus Capsid from Isolate Rhesus 32.33. *J. Virol.* 87, 9473–9485. <https://doi.org/10.1128/jvi.00596-13>.
35. Russell, S., Bennett, J., Wellman, J.A., Chung, D.C., Yu, Z.-F., Tillman, A., Wittes, J., Pappas, J., Elci, O., McCague, S., et al. (2017). Efficacy and safety of voretigene neparvovec (AAV2-hRPE65v2) in patients with RPE65-mediated inherited retinal dystrophy: a randomised, controlled, open-label, phase 3 trial. *Lancet* 390, 849–860. [https://doi.org/10.1016/S0140-6736\(17\)31868-8](https://doi.org/10.1016/S0140-6736(17)31868-8).
36. Lek, A., Wong, B., Keeler, A., Blackwood, M., Ma, K., Huang, S., Sylvia, K., Batista, A.R., Artinian, R., Kokoski, D., et al. (2023). Death after High-Dose rAAV9 Gene Therapy in a Patient with Duchenne's Muscular Dystrophy. *N. Engl. J. Med.* 389, 1203–1210. <https://doi.org/10.1056/NEJMoa2307798>.
37. Wu, Z., Asokan, A., and Samulski, R.J. (2006). Adeno-associated Virus Serotypes: Vector Toolkit for Human Gene Therapy. *Mol. Ther.* 14, 316–327. <https://doi.org/10.1016/j.ymthe.2006.05.009>.
38. Asokan, A., Schaffer, D.V., and Samulski, R.J. (2012). The AAV Vector Toolkit: Poised at the Clinical Crossroads. *Mol. Ther.* 20, 699–708. <https://doi.org/10.1038/mt.2011.287>.
39. Pupo, A., Fernández, A., Low, S.H., François, A., Suárez-Amarán, L., and Samulski, R.J. (2022). AAV vectors: The Rubik's cube of human gene therapy. *Mol. Ther.* 30, 3515–3541. <https://doi.org/10.1016/j.ymthe.2022.09.015>.
40. Shen, X., Storm, T., and Kay, M.A. (2007). Characterization of the Relationship of AAV Capsid Domain Swapping to Liver Transduction Efficiency. *Mol. Ther.* 15, 1955–1962. <https://doi.org/10.1038/sj.mt.6300293>.
41. Hauck, B., and Xiao, W. (2003). Characterization of Tissue Tropism Determinants of Adeno-Associated Virus Type 1. *J. Virol.* 77, 2768–2774. <https://doi.org/10.1128/jvi.77.4.2768-2774.2003>.



42. Havlik, L.P., Simon, K.E., Smith, J.K., Klinc, K.A., Tse, L.V., Oh, D.K., Fanous, M.M., Meganck, R.M., Mietzsch, M., Kleinschmidt, J., et al. (2020). Coevolution of Adeno-associated Virus Capsid Antigenicity and Tropism through a Structure-Guided Approach. *J. Virol.* *94*, e00976-20. <https://doi.org/10.1128/jvi.00976-00920>.
43. Raupp, C., Naumer, M., Müller, O.J., Gurda, B.L., Agbandje-McKenna, M., and Kleinschmidt Jürgen, A. (2012). The Threefold Protrusions of Adeno-Associated Virus Type 8 Are Involved in Cell Surface Targeting as Well as Postattachment Processing. *J. Virol.* *86*, 9396–9408. <https://doi.org/10.1128/jvi.00209-12>.
44. Strassheim, M.L., Gruenberg, A., Vejjalainen, P., Sgro, J.-Y., and Parrish, C.R. (1994). Two Dominant Neutralizing Antigenic Determinants of Canine Parvovirus Are Found on the Threefold Spike of the Virus Capsid. *Virology* *198*, 175–184. <https://doi.org/10.1006/viro.1994.1020>.
45. Wobus, C.E., Hügler-Dörr, B., Girod, A., Petersen, G., Hallek, M., and Kleinschmidt Jürgen, A. (2000). Monoclonal Antibodies against the Adeno-Associated Virus Type 2 (AAV-2) Capsid: Epitope Mapping and Identification of Capsid Domains Involved in AAV-2-Cell Interaction and Neutralization of AAV-2 Infection. *J. Virol.* *74*, 9281–9293. <https://doi.org/10.1128/jvi.74.19.9281-9293.2000>.
46. Tseng, Y.-S., and Agbandje-McKenna, M. (2014). Mapping the AAV Capsid Host Antibody Response toward the Development of Second Generation Gene Delivery Vectors. *Front. Immunol.* *5*, 9. <https://doi.org/10.3389/fimmu.2014.00009>.
47. Hsu, H.-L., Brown, A., Loveland, A.B., Lotun, A., Xu, M., Luo, L., Xu, G., Li, J., Ren, L., Su, Q., et al. (2020). Structural characterization of a novel human adeno-associated virus capsid with neurotropic properties. *Nat. Commun.* *11*, 3279. <https://doi.org/10.1038/s41467-020-17047-1>.
48. Ronzitti, G., Gross, D.-A., and Mingozzi, F. (2020). Human Immune Responses to Adeno-Associated Virus (AAV) Vectors. *Front. Immunol.* *11*, 670. <https://doi.org/10.3389/fimmu.2020.00670>.
49. Abbink, P., Maxfield, L.F., Ng'ang'a, D., Borducchi, E.N., Iampietro, M.J., Bricault, C.A., Teigler, J.E., Blackmore, S., Parenteau, L., Wagh, K., et al. (2015). Construction and Evaluation of Novel Rhesus Monkey Adenovirus Vaccine Vectors. *J. Virol.* *89*, 1512–1522. <https://doi.org/10.1128/jvi.02950-14>.
50. Abbink, P., Kirilova, M., Boyd, M., Mercado, N., Li, Z., Nityanandam, R., Nanayakkara, O., Peterson, R., Larocca, R.A., Aid, M., et al. (2018). Rapid Cloning of Novel Rhesus Adenoviral Vaccine Vectors. *J. Virol.* *92*, e01924-17. <https://doi.org/10.1128/jvi.01924-01917>.
51. Fripont, S., Marneffe, C., Marino, M., Rincon, M.Y., and Holt, M.G. (2019). Production, Purification, and Quality Control for Adeno-associated Virus-based Vectors. *J. Vis. Exp.* *143*, e58960. <https://doi.org/10.3791/58960>.
52. Mastronarde, D.N. (2005). Automated electron microscope tomography using robust prediction of specimen movements. *J. Struct. Biol.* *152*, 36–51. <https://doi.org/10.1016/j.jsb.2005.07.007>.
53. Zheng, S.Q., Palovcak, E., Armache, J.P., Verba, K.A., Cheng, Y., and Agard, D.A. (2017). MotionCor2: anisotropic correction of beam-induced motion for improved cryo-electron microscopy. *Nat. Methods* *14*, 331–332. <https://doi.org/10.1038/nmeth.4193>.
54. Grant, T., Rohou, A., and Grigorieff, N. (2018). cisTEM, user-friendly software for single-particle image processing. *Elife* *7*, e35383. <https://doi.org/10.7554/eLife.35383>.
55. Lucas, B.A., Himes, B.A., Xue, L., Grant, T., Mahamid, J., and Grigorieff, N. (2021). Locating macromolecular assemblies in cells by 2D template matching with cisTEM. *Elife* *10*, e68946. <https://doi.org/10.7554/eLife.68946>.
56. Punjani, A., Rubinstein, J.L., Fleet, D.J., and Brubaker, M.A. (2017). cryoSPARC: algorithms for rapid unsupervised cryo-EM structure determination. *Nat. Methods* *14*, 290–296. <https://doi.org/10.1038/nmeth.4169>.
57. Zhang, K. (2016). Gctf: Real-time CTF determination and correction. *J. Struct. Biol.* *193*, 1–12. <https://doi.org/10.1016/j.jsb.2015.11.003>.
58. Scheres, S.H.W. (2012). RELION: implementation of a Bayesian approach to cryo-EM structure determination. *J. Struct. Biol.* *180*, 519–530. <https://doi.org/10.1016/j.jsb.2012.09.006>.
59. Scheres, S.H. (2014). Beam-induced motion correction for sub-megadalton cryo-EM particles. *Elife* *3*, e03665. <https://doi.org/10.7554/eLife.03665>.
60. Lyumkis, D., Brilot, A.F., Theobald, D.L., and Grigorieff, N. (2013). Likelihood-based classification of cryo-EM images using FREALIGN. *J. Struct. Biol.* *183*, 377–388. <https://doi.org/10.1016/j.jsb.2013.07.005>.
61. Afonine, P.V. (2017). phenix.mtriage: a tool for analysis and validation of cryo-EM 3D reconstructions. *Computational Crystallography Newsletter* *8*, 25.
62. Jumper, J., Evans, R., Pritzel, A., Green, T., Figurnov, M., Ronneberger, O., Tunyasuvunakool, K., Bates, R., Židek, A., Potapenko, A., et al. (2021). Highly accurate protein structure prediction with AlphaFold. *Nature* *596*, 583–589. <https://doi.org/10.1038/s41586-021-03819-2>.
63. Afonine, P.V., Poon, B.K., Read, R.J., Sobolev, O.V., Terwilliger, T.C., Urzhumtsev, A., and Adams, P.D. (2018). Real-space refinement in PHENIX for cryo-EM and crystallography. *Acta Crystallogr. D Struct. Biol.* *74*, 531–544. <https://doi.org/10.1107/S2059798318006551>.
64. Jones, T.A., Zou, J.Y., Cowan, S.W., and Kjeldgaard, M. (1991). Improved methods for building protein models in electron density maps and the location of errors in these models. *Acta Crystallogr. A* *47*, 110–119.
65. Emsley, P., and Cowtan, K. (2004). Coot: model-building tools for molecular graphics. *Acta Crystallogr. D Biol. Crystallogr.* *60*, 2126–2132. <https://doi.org/10.1107/S0907444904019158>.
66. Chen, V.B., Arendall, W.B., 3rd, Headd, J.J., Keedy, D.A., Immormino, R.M., Kapral, G.J., Murray, L.W., Richardson, J.S., and Richardson, D.C. (2010). MolProbity: all-atom structure validation for macromolecular crystallography. *Acta Crystallogr. D Biol. Crystallogr.* *66*, 12–21. <https://doi.org/10.1107/S0907444909042073>.
67. Hunter, J.D. (2007). Matplotlib: A 2D graphics environment. *Comput. Sci. Eng.* *9*, 90–95.
68. Krotova, K., and Aslanidi, G. (2020). Modifiers of Adeno-Associated Virus-Mediated Gene Expression in Implication for Serotype-Universal Neutralizing Antibody Assay. *Hum. Gene Ther.* *31*, 1124–1131. <https://doi.org/10.1089/hum.2020.074>.
69. Cadena, A.M., Ventura, J.D., Abbink, P., Borducchi, E.N., Tuyishime, H., Mercado, N.B., Walker-Sperling, V., Siamatu, M., Liu, P.-T., Chandrashekar, A., et al. (2021). Persistence of viral RNA in lymph nodes in ART-suppressed SIV/SHIV-infected Rhesus Macaques. *Nat. Commun.* *12*, 1474. <https://doi.org/10.1038/s41467-021-21724-0>.
70. Schmittgen, T.D., and Livak, K.J. (2008). Analyzing real-time PCR data by the comparative CT method. *Nat. Protoc.* *3*, 1101–1108. <https://doi.org/10.1038/nprot.2008.73>.